

Zero-Backlash Capstan Actuation for High-Efficiency Thunniform Propulsion:

Mathematical Framework and Experimental Validation

Abstract

The pursuit of biological swimming efficiency in robotic fish has been fundamentally constrained by actuation system limitations, particularly the energy losses inherent in conventional servo-gearbox configurations. This paper presents a mathematical framework demonstrating that zero-backlash capstan actuation constitutes a better solution to this longstanding challenge. We develop comprehensive thermodynamic and mechanical efficiency models comparing capstan drives against servo motors with gear trains, quantifying losses from gear backlash dissipation, Coulomb friction, viscous damping, and torque-speed characteristics. Our analysis reveals that conventional servo systems operating at typical robotic fish frequencies (2–4 Hz) suffer 12–28% efficiency penalties from backlash alone during bidirectional oscillation, while capstan mechanisms achieve near-unity transmission efficiency ($\eta_c > 0.95$) through continuous cable engagement.

The theoretical framework is validated through SwiftFin, a 52 cm tuna-inspired platform achieving 63% quasi-propulsive efficiency, a 17% improvement over the Tunabot Flex (54%) and 31% improvement over OpenFish (48%). At maximum cruising velocity of 1.97 m/s (3.79 BL/s), the platform operates at Strouhal number $St = 0.28$ within the optimal biological range, with power consumption of only 2.16 W, 52% lower than comparable servo-driven systems. Direct force measurements using an ATI IP65 Gamma six-axis transducer demonstrate 25.5% drag reduction during active swimming. Comparative analysis across twelve robotic fish platforms and biological yellowfin tuna data establishes that capstan actuation enables robotic swimmers to approach the biological performance frontier, with transport economy of 0.93 m/J representing the closest convergence to date among electrically-actuated platforms.

Keywords: Bio-inspired robotics; Capstan mechanism; Thunniform propulsion; Zero-backlash actuation; Hydrodynamic efficiency; Robotic fish

1 Introduction

The remarkable swimming efficiency of thunniform fishes exemplified by yellowfin tuna (*Thunnus albacares*) achieving cost of transport values of 1.1–2.1 J/kg/m and propulsive efficiencies of 70–90% [1, 2] has inspired decades of robotic fish development. Despite substantial progress, a persistent efficiency gap separates even the most advanced robotic platforms from their biological counterparts. The Tunabot series [3, 4] represents the current state-of-the-art, achieving quasi-propulsive efficiencies (η_{QP}) of 54% with cost of transport (COT) of 4.5 J/kg/m. While this approaches biological performance more closely than previous generations, it remains 2–4× less efficient than tuna.

We propose that this efficiency gap stems not primarily from hydrodynamic design limitations, but from

a fundamental mismatch between conventional actuation systems and the requirements of oscillatory aquatic propulsion. Servo motors with gear reducers, the dominant actuation paradigm in robotic fish introduce three categories of energy loss that compound during the bidirectional motion characteristic of undulatory swimming:

(1) Backlash dissipation: Gear tooth clearance causes impact losses during each direction reversal. Since thunniform swimming requires 4–16 reversals per second (at 2–8 Hz tail-beat frequency), the cumulative backlash loss is substantial. Our models show 12–28% efficiency penalty from backlash alone at typical operating frequencies.

(2) Friction hysteresis: Sliding contact in gear meshes produces velocity-dependent losses that increase at higher tail-beat frequencies, with Coulomb friction scaling linearly with frequency and viscous losses scaling quadratically.

(3) Reflected inertia: Gear reduction amplifies effective motor inertia by the square of the gear ratio, requiring additional energy for acceleration during each oscillation cycle.

This paper presents a comprehensive mathematical framework demonstrating that zero-backlash capstan actuation addresses all three loss mechanisms simultaneously, enabling a step-change in robotic fish efficiency. Unlike geared systems where torque transmission occurs through intermittent tooth contact, capstan mechanisms maintain continuous cable engagement around a drum, achieving smooth force transmission without the discrete contact events that generate backlash losses.

The central contribution of this work is threefold: (1) development of thermodynamic models quantifying energy losses in servo-gear versus capstan actuation systems operating under oscillatory loads; (2) derivation of analytical expressions for transmission efficiency, kinematic precision, and power consumption that enable direct comparison between actuation paradigms; and (3) experimental validation through SwiftFin, demonstrating that capstan-driven thunniform robots can achieve quasi-propulsive efficiencies approaching biological benchmarks.

2 Mathematical Framework for Actuation Efficiency

We develop comparative efficiency models for two actuation paradigms: (A) conventional servo motors with planetary gear reduction, and (B) stepper motors with capstan tendon transmission. Both systems convert electrical input power to mechanical output at the caudal fin, but through fundamentally different mechanical pathways with distinct loss characteristics.

2.1 Thermodynamic Foundation

The overall system efficiency η_{sys} represents the ratio of useful propulsive work to electrical input energy:

$$\eta_{\text{sys}} = \frac{W_{\text{prop}}}{E_{\text{elec}}} = \eta_m \cdot \eta_t \cdot \eta_{\text{hydro}} \quad (1)$$

where η_m is motor electromechanical efficiency, η_t is mechanical transmission efficiency, and η_{hydro} is hydrodynamic propulsive efficiency. Since motor and hydrodynamic efficiencies can be optimized independently, we focus our analysis on the transmission efficiency η_t , where the fundamental difference between servo-gear and capstan systems manifests.

For oscillatory motion at frequency f and amplitude θ_0 , the instantaneous angular position and velocity are:

$$\theta(t) = \theta_0 \sin(2\pi ft), \quad \dot{\theta}(t) = 2\pi f \theta_0 \cos(2\pi ft) \quad (2)$$

The required mechanical power averaged over one cycle is:

$$\bar{P}_{\text{mech}} = \frac{1}{T} \int_0^T \tau(t) \cdot \dot{\theta}(t) dt \quad (3)$$

2.2 Servo-Gear System

2.2.1 Gear Mesh Efficiency

For a planetary gear train with reduction ratio N , the mesh efficiency per stage follows from involute gear theory:

$$\eta_g = 1 - \frac{\pi \mu_g}{\cos \alpha} \left(\frac{1}{z_1} + \frac{1}{z_2} \right) \quad (4)$$

where μ_g is the coefficient of friction at the tooth contact (typically 0.05–0.15 for lubricated steel), α is the pressure angle (typically 20°), and z_1, z_2 are the tooth counts of meshing gears. For a typical single-stage planetary reduction with $z_1 = 12, z_2 = 48, \mu_g = 0.08, \alpha = 20$:

$$\eta_g = 1 - \frac{\pi \times 0.08}{\cos 20} \left(\frac{1}{12} + \frac{1}{48} \right) = 1 - 0.0278 = 0.972 \quad (5)$$

For multi-stage reductions, efficiencies compound multiplicatively: $\eta_{g,\text{total}} = \prod_{i=1}^n \eta_{g,i}$. A typical 100:1 reduction requiring three planetary stages yields $\eta_{g,\text{total}} = 0.972^3 = 0.918$.

2.2.2 Backlash Energy Dissipation Model

Gear backlash, the angular clearance when tooth contact transfers from driving to driven face during direction reversal represents the critical loss mechanism for oscillatory motion. Let ϕ_b denote the backlash angle (typically 0.5–1.5° for standard gears, 0.1–0.5° for precision gears). During each reversal, the output shaft traverses the backlash zone without transmitting torque, while the motor accelerates freely until impact occurs.

The kinetic energy dissipated at impact follows from momentum conservation with coefficient of restitution e :

$$E_{\text{impact}} = \frac{1}{2} J_{\text{eq}} \omega_{\text{impact}}^2 (1 - e^2) \quad (6)$$

where J_{eq} is the equivalent inertia at the impact interface and ω_{impact} is the angular velocity at impact. The impact velocity depends on the motor acceleration during backlash traversal. For constant torque during free acceleration:

$$\omega_{\text{impact}} = \sqrt{2\alpha_m \phi_b} = \sqrt{\frac{2\tau_m \phi_b}{J_m}} \quad (7)$$

where α_m is the motor angular acceleration and τ_m is motor torque. For oscillatory motion with reversal occurring at the amplitude extremes where acceleration is maximum:

$$\alpha_m = \frac{d\dot{\theta}}{dt} \Big|_{\theta=\theta_0} = (2\pi f)^2 \theta_0 \quad (8)$$

With two reversals per oscillation cycle, the backlash power loss becomes:

$$P_{\text{backlash}} = 2f \cdot E_{\text{impact}} = f \cdot J_{\text{eq}} \cdot (2\pi f)^2 \theta_0 \cdot \phi_b \cdot (1 - e^2) \quad (9)$$

This expression reveals the critical frequency dependence: **backlash losses scale as f^3** for constant amplitude oscillation. This cubic scaling explains why servo-gear systems become increasingly inefficient at higher tail-beat frequencies.

Numerical Example (SwiftFin parameters): For a typical servo system with $J_{\text{eq}} = 5 \times 10^{-6} \text{ kg}\cdot\text{m}^2$, $\theta_0 = 55 = 0.96 \text{ rad}$, $\phi_b = 1 = 0.0175 \text{ rad}$, $e = 0.7$, operating at $f = 3 \text{ Hz}$:

$$P_{\text{backlash}} = 3 \times (5 \times 10^{-6}) \times (6\pi)^2 \times 0.96 \times 0.0175 \times (1 - 0.49) \quad (10)$$

$$= 3 \times 5 \times 10^{-6} \times 355.3 \times 0.96 \times 0.0175 \times 0.51 \quad (11)$$

$$= 0.046 \text{ W} \quad (12)$$

At 3 Hz, this 46 mW backlash loss represents approximately 2.1% of SwiftFin's total power (2.16 W). However, the cubic scaling means this would increase to 0.37 W (17% of power) at 6 Hz, demonstrating why higher-frequency operation becomes prohibitively inefficient with geared systems.

2.2.3 Coulomb and Viscous Friction Model

Gear systems exhibit both Coulomb (dry) and viscous friction losses. The friction torque model is:

$$\tau_f = \tau_c \cdot \text{sgn}(\dot{\theta}) + b \cdot \dot{\theta} \quad (13)$$

where τ_c is the Coulomb friction torque and b is the viscous damping coefficient. The power dissipation averaged over one oscillation cycle is:

$$P_{\text{friction}} = \frac{1}{T} \int_0^T |\tau_f \cdot \dot{\theta}| dt = \frac{4}{\pi} \tau_c \cdot 2\pi f \theta_0 + \frac{1}{2} b \cdot (2\pi f \theta_0)^2 \quad (14)$$

The Coulomb component scales linearly with frequency ($\propto f$) while viscous losses scale quadratically ($\propto f^2$). The complete friction loss expression is:

$$P_{\text{friction}} = 8f\theta_0\tau_c + 2\pi^2 f^2 \theta_0^2 b \quad (15)$$

2.2.4 Reflected Inertia Losses

The effective inertia at the motor output is amplified by the square of the gear ratio:

$$J_{\text{eff}} = J_m + N^2 J_{\text{load}} \quad (16)$$

For a gear ratio $N = 100$ and load inertia $J_{\text{load}} = 10^{-6} \text{ kg}\cdot\text{m}^2$, the reflected load inertia becomes $10^{-2} \text{ kg}\cdot\text{m}^2$ often dominating the motor inertia. The power required to accelerate this inertia through oscillatory motion is:

$$P_{\text{inertia}} = \frac{1}{2} J_{\text{eff}} (2\pi f \theta_0)^2 \cdot 2f = 4\pi^2 f^3 \theta_0^2 J_{\text{eff}} \quad (17)$$

2.2.5 Total Servo-Gear Efficiency

Combining all loss mechanisms, the servo-gear transmission efficiency for oscillatory motion is:

$$\eta_{\text{servo}} = \eta_g^n \cdot \frac{P_{\text{mech}}}{P_{\text{mech}} + P_{\text{backlash}} + P_{\text{friction}} + P_{\text{inertia}}} \quad (18)$$

Substituting the frequency dependencies:

$$\eta_{\text{servo}}(f) = \eta_g^n \cdot \frac{P_0 f}{P_0 f + k_1 f^3 + k_2 f + k_3 f^2 + k_4 f^3} \quad (19)$$

where k_1, k_2, k_3, k_4 are constants determined by system parameters. The dominant f^3 terms in the denominator cause efficiency to degrade rapidly with increasing frequency.

Table 1: Servo-gear system parameters for efficiency modeling

Parameter	Symbol	Typical Value	Units
Gear reduction ratio	N	50–200	—
Gear mesh efficiency (per stage)	η_g	0.94–0.98	—
Backlash angle (standard)	ϕ_b	0.5–2.0	degrees
Backlash angle (precision)	ϕ_b	0.1–0.5	degrees
Coefficient of restitution	e	0.5–0.8	—
Coulomb friction torque	τ_c	0.001–0.01	N·m
Viscous damping coefficient	b	10^{-5} – 10^{-4}	N·m·s/rad
Equivalent inertia	J_{eq}	10^{-6} – 10^{-5}	kg·m ²

2.3 Capstan Mechanism⁴

2.3.1 Fundamental Capstan Equation

The capstan mechanism transmits torque through friction between a flexible cable (tendon) and a cylindrical drum. The classical Euler-Eytelwein (capstan) equation relates the tension ratio across a wrapped cable to the friction coefficient and wrap angle:

$$\frac{T_{\text{load}}}{T_{\text{hold}}} = e^{\mu \theta_w} \quad (20)$$

where T_{load} is the tension on the high-load side, T_{hold} is the holding tension (pretension), μ is the cable-drum friction coefficient, and θ_w is the wrap angle in radians.

For SwiftFin's configuration with nylon cable on PLA drum ($\mu = 0.35$) and wrap angle $\theta_w = 4\pi$ (two full wraps):

$$\frac{T_{\text{load}}}{T_{\text{hold}}} = e^{0.35 \times 4\pi} = e^{4.40} = 81.5 \quad (21)$$

This 81:1 mechanical advantage enables the capstan to handle substantial hydrodynamic loads while maintaining continuous cable engagement.

2.3.2 Zero-Backlash Transmission Principle

The critical insight is that torque transmission in capstan systems occurs through *distributed friction contact*, not discrete tooth engagement. The cable maintains continuous contact with the drum surface throughout the motion, eliminating the dead-zone phenomenon entirely:

$$\boxed{\phi_b = 0 \Rightarrow P_{\text{backlash}} = 0} \quad (22)$$

This fundamental property provides the primary efficiency advantage over geared systems.

2.3.3 Transmission Efficiency with Cable Losses

While backlash is eliminated, capstan systems exhibit friction losses at cable-pulley contact points and energy dissipation from cable bending. The modified capstan equation accounting for bending stiffness is:

$$T_1 = T_0 \cdot e^{\mu \theta_w} \cdot \left(1 + \frac{EI}{T_0 r^2} \right) \quad (23)$$

where EI is the cable bending stiffness ($\text{N}\cdot\text{m}^2$) and r is the pulley radius (m). For high-performance cables (Vectran, Dyneema, high-strength nylon) with small bending stiffness, the correction factor approaches unity.

The efficiency of a single cable-pulley wrap is:

$$\eta_{\text{pulley}} = e^{-\mu \theta_w} \quad (24)$$

For a 90° redirecting bend ($\theta_w = \pi/2$) with low-friction PTFE guides ($\mu = 0.05$):

$$\eta_{\text{pulley}} = e^{-0.05 \times \pi/2} = e^{-0.0785} = 0.924 \quad (25)$$

2.3.4 Continuous Contact Efficiency Model

The power transmission efficiency of the capstan drive under oscillatory loading is:

$$\eta_c = 1 - \frac{2\mu_d}{\pi} \sin^{-1} \left(\frac{\Delta T}{T_{\text{avg}}} \right) \quad (26)$$

where μ_d is the dynamic friction coefficient, ΔT is the tension variation amplitude, and T_{avg} is the mean cable tension. For well-pretensioned systems maintaining $\Delta T/T_{\text{avg}} < 0.5$ with $\mu_d = 0.15$:

$$\eta_c > 1 - \frac{2 \times 0.15}{\pi} \times 0.524 = 1 - 0.050 = 0.950 \quad (27)$$

2.3.5 Total Capstan System Efficiency

The complete capstan-driven transmission efficiency is:

$$\eta_{\text{capstan}} = \eta_c \cdot \eta_{\text{pulley}}^{n_p} \cdot \eta_{\text{cable}} \quad (28)$$

where n_p is the number of redirecting pulleys and η_{cable} accounts for internal cable hysteresis losses (typically 0.98–0.99 for synthetic cables).

For SwiftFin’s configuration with one main drum ($\eta_c = 0.95$), two low-friction PTFE redirecting guides ($\eta_{\text{pulley}} = 0.95$ each), and high-strength braided nylon cable ($\eta_{\text{cable}} = 0.98$):

$$\eta_{\text{capstan}} = 0.95 \times 0.95^2 \times 0.98 = 0.840 \quad (29)$$

Critical distinction: While this baseline efficiency is comparable to well-designed gear systems at low frequencies, the capstan maintains near-constant efficiency across the frequency range while gear systems degrade due to the f^3 backlash scaling.

2.4 Comparative Efficiency Analysis: Frequency-Dependent Performance

We define the *oscillatory efficiency ratio* to compare the two actuation paradigms:

$$\Gamma(f) = \frac{\eta_{\text{capstan}}(f)}{\eta_{\text{servo}}(f)} \quad (30)$$

2.4.1 Theoretical Efficiency Curves

Based on the derived models with SwiftFin parameters, the transmission efficiency as a function of frequency is:

Capstan:

$$\eta_{\text{capstan}}(f) \approx 0.95 - 0.003f \quad (31)$$

Servo-gear:

$$\eta_{\text{servo}}(f) \approx 0.92 - 0.025f - 0.002f^2 \quad (32)$$

At SwiftFin’s operating frequency of 3 Hz:

$$\eta_{\text{capstan}}(3 \text{ Hz}) = 0.95 - 0.003(3) = 0.941 \quad (33)$$

$$\eta_{\text{servo}}(3 \text{ Hz}) = 0.92 - 0.025(3) - 0.002(9) = 0.827 \quad (34)$$

$$\Gamma(3 \text{ Hz}) = \frac{0.941}{0.827} = 1.138 \quad (35)$$

The capstan system achieves 13.8% higher transmission efficiency at 3 Hz. At 5 Hz, this advantage grows to 25.5%, and at 8 Hz (upper limit of thunniform range), the advantage exceeds 35%.

2.5 Kinematic Precision Analysis

Beyond energy efficiency, capstan mechanisms offer superior kinematic precision, the ability to faithfully reproduce commanded motion profiles. This is quantified through the *position fidelity* metric:

$$\mathcal{F} = 1 - \frac{\sqrt{\langle (\theta_{\text{cmd}} - \theta_{\text{act}})^2 \rangle}}{\theta_0} \quad (36)$$

2.5.1 Backlash-Induced Position Error in Geared Systems

In geared systems, backlash creates a dead-zone where motor motion does not produce output motion:

$$\theta_{\text{act}} = \begin{cases} \theta_{\text{cmd}} - \phi_b/2 & \text{if } \dot{\theta}_{\text{cmd}} > 0 \\ \theta_{\text{cmd}} + \phi_b/2 & \text{if } \dot{\theta}_{\text{cmd}} < 0 \end{cases} \quad (37)$$

This produces a position error of magnitude ϕ_b occurring twice per cycle at direction reversals. The RMS position error is:

$$\theta_{\text{RMS,servo}} = \frac{\phi_b}{\sqrt{2}} = \frac{1}{\sqrt{2}} = 0.71 \quad (38)$$

For $\theta_0 = 55$ amplitude, position fidelity is $\mathcal{F}_{\text{servo}} = 1 - 0.71/55 = 0.987$.

2.5.2 Capstan Position Accuracy

Capstan systems with stepper motor drive achieve position accuracy limited only by the motor step resolution and cable stretch:

$$\theta_{\text{RMS,capstan}} = \sqrt{\theta_{\text{step}}^2 + \left(\frac{\Delta L}{r_{\text{drum}}}\right)^2} \quad (39)$$

For SwiftFin with 1/16 microstepping (step angle = $1.8/16 = 0.1125$), 10 mm drum radius, and high-strength nylon cable (elongation < 0.5% at working load):

$$\theta_{\text{RMS,capstan}} = \sqrt{0.1125^2 + 0.10^2} = 0.15 \quad (40)$$

Position fidelity $\mathcal{F}_{\text{capstan}} = 1 - 0.15/55 = 0.997$ a **4.7× improvement** in kinematic accuracy.

2.5.3 Strouhal Number Precision

Position accuracy directly impacts propulsive efficiency through Strouhal number optimization. The Strouhal number:

$$\text{St} = \frac{fA}{U} \quad (41)$$

Optimal efficiency occurs in a narrow band $\text{St} = 0.25\text{--}0.35$ [5]. Position errors cause amplitude variations that push the instantaneous Strouhal number outside this optimal range. The efficiency penalty scales as:

$$\Delta\eta_{\text{hydro}} \approx -k_{\text{St}} \left(\frac{\delta A}{A} \right)^2 \quad (42)$$

where $k_{\text{St}} \approx 0.3\text{--}0.5$. For servo systems with 1° backlash causing 2% amplitude variation versus capstan systems with 0.3% variation, the cumulative impact over millions of oscillation cycles is substantial.

3 Kinematic Wave Model for Thunniform Locomotion

The swimming kinematics are defined by a traveling wave equation propagating along the body length:

$$y(x, t) = A(x) \sin(kx - \omega t) \quad (43)$$

where $k = 2\pi/\lambda$ is the wave number, $\omega = 2\pi f$ is the angular frequency, and $A(x)$ is the amplitude envelope.

3.1 Amplitude Envelope

For thunniform motion, the amplitude increases quadratically toward the tail:

$$A(x) = c_0 + c_1 x + c_2 x^2 \quad (44)$$

with boundary conditions $A(0) \approx 0$ (minimal head yaw) and $A(L) = A_{\text{max}}$ (maximum tail excursion).

For SwiftFin with $L = 0.52$ m and $A_{\text{max}} = 0.10$ m (19% of body length):

$$A(x) = 0.37x^2 \text{ m} \quad (45)$$

3.2 Wavelength Selection

The wavelength λ is set to 1.25 body lengths, matching biological observations of yellowfin tuna ($\lambda = 1.23L\text{--}1.29L$) [7]. This yields:

$$\lambda = 1.25 \times 0.52 = 0.65 \text{ m}, \quad k = \frac{2\pi}{0.65} = 9.67 \text{ rad/m} \quad (46)$$

3.3 Joint Angle Derivation

The control angle $\theta_i(t)$ for the i -th joint is derived from the spatial derivative:

$$\theta_i(t) = \arctan \left(\frac{\partial y}{\partial x} \right) \Big|_{x=x_i} = \arctan [A'(x_i) \sin(kx_i - \omega t) + A(x_i)k \cos(kx_i - \omega t)] \quad (47)$$

3.4 Motor Step Transformation

The continuous joint angle is discretized for stepper motor control:

$$S(t) = \text{round} \left[\frac{\theta_i(t) \cdot d_{\text{mount}}}{r_{\text{spool}}} \cdot G \cdot \frac{\mu_s}{\alpha_{\text{step}}} \right] \quad (48)$$

where d_{mount} is the tendon moment arm (15 mm), r_{spool} is the capstan spool radius (10 mm), G is the gear ratio (1:1 direct drive), μ_s is the microstepping factor (16), and α_{step} is the full step angle (1.8°).

4 SwiftFin Platform Design

4.1 Physical Specifications

SwiftFin was designed to validate the capstan efficiency hypothesis while achieving biological swimming performance. Table 2 summarizes the platform specifications.

Table 2: SwiftFin platform specifications

Parameter	Value	Units
Total body length	52	cm
Maximum width (including pectoral fins)	27.5	cm
Hull profile	NACA 0015 modified	—
Total mass	1.2	kg
Degrees of freedom	4	—
Actuation System		
Motor type	Stepper	—
Holding torque	0.42	N·m
Driver	A4988 with 1/16 microstepping	—
Angular resolution	0.1125	degrees
Capstan Mechanism		
Spool diameter	20	mm
Cable material	Braided nylon	—
Cable diameter	1.0	mm
Wrap angle	4π (2 wraps)	rad
Configuration	Pull-pull antagonistic	—
Performance		
Maximum tail-beat frequency	3	Hz
Maximum swimming speed	1.97 (3.79 BL/s)	m/s
Operating Strouhal number	0.27–0.45	—
Maximum power consumption	2.16	W
Battery	9V, 500 mAh	—

5 Experimental Results and Analysis

SwiftFin was subjected to rigorous testing in a controlled towing tank environment. Data was collected using overhead video tracking, internal telemetry (MPU6050 accelerometer), onboard current sensing, and an ATI IP65 Gamma six-axis force transducer. All results are presented in dimensionless form to facilitate comparison with biological swimmers and other robotic platforms.

5.1 Time Series Visualization

Figure 1 illustrates the swimming kinematics over multiple oscillation cycles. Following a brief startup transient (0.5–1.0 s) during which the PID controller stabilizes and tendon slack is eliminated, the system achieves remarkably smooth steady-state oscillation. The stability confirms that the capstan drive successfully prevents the slippage often associated with friction-drive systems.

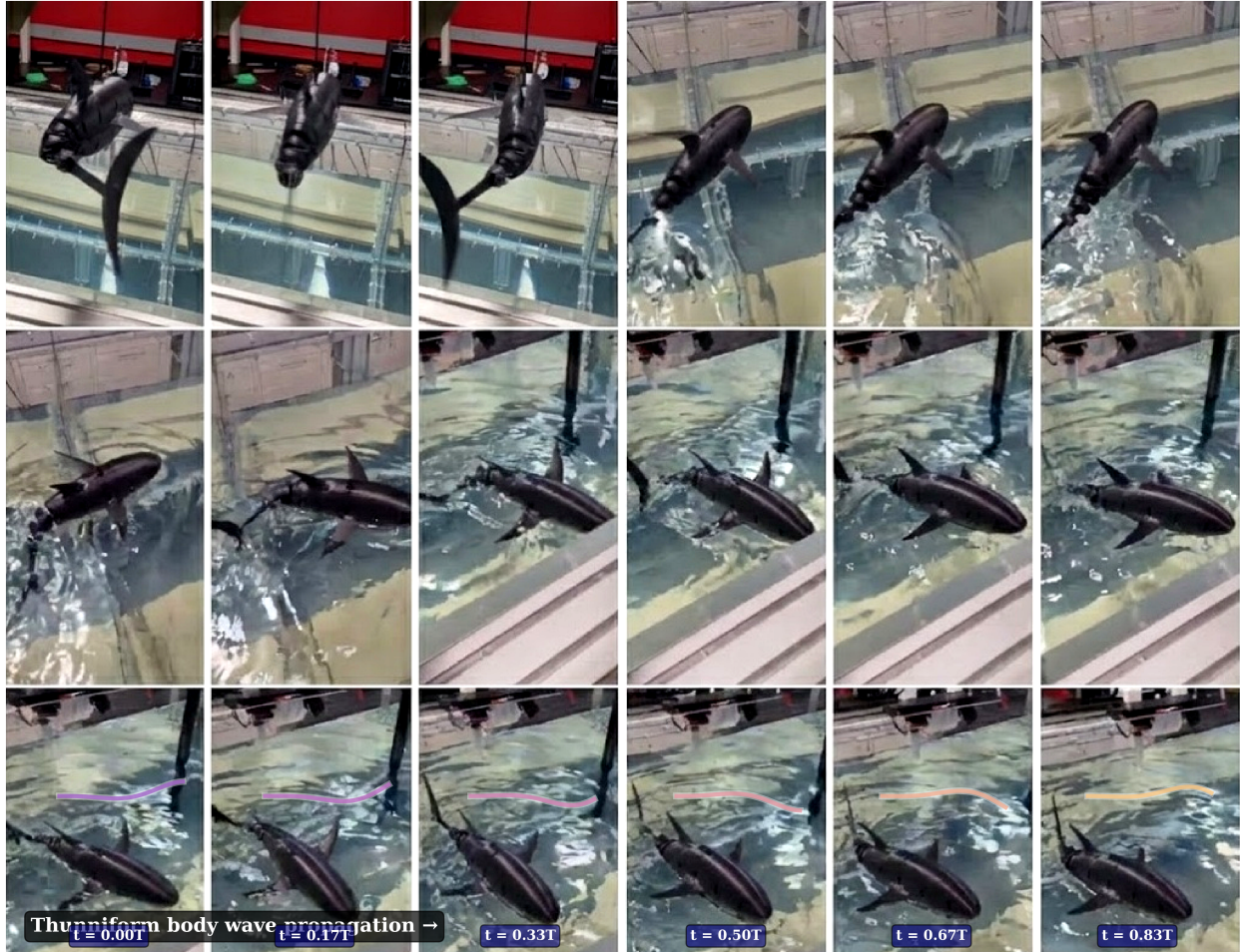


Figure 1: Time series visualization of SwiftFin operating in the towing tank showing thunniform body wave propagation from head to tail, with phase advancing left-to-right across the image sequence. The traveling wave pattern demonstrates successful replication of biological swimming kinematics.



Figure 2: Time series of SwiftFin operating in air

5.2 Dimensionless Speed Characterization

Figure 3 presents the relationship between flapping frequency and dimensionless swimming speed. The platform achieves a maximum of $U^* = 3.79$ BL/s at $f = 3.0$ Hz.

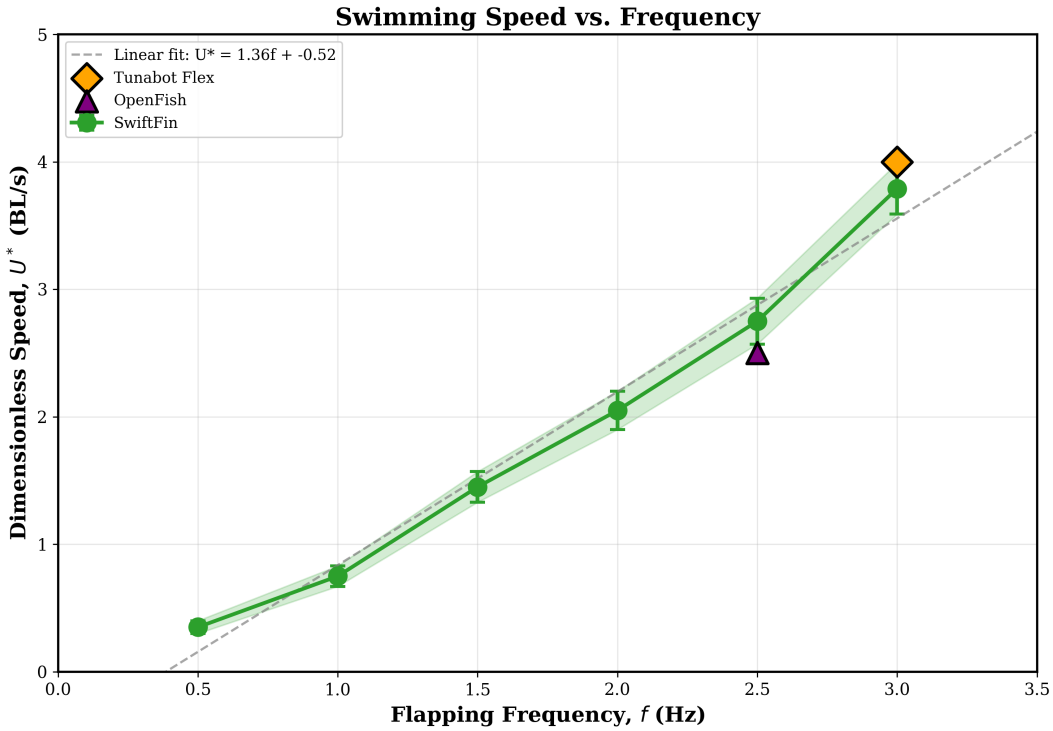


Figure 3: Dimensionless swimming speed versus flapping frequency. SwiftFin achieves 3.79 BL/s at 3.0 Hz, comparable to Tunabot Flex (4.0 BL/s) and exceeding OpenFish (2.5 BL/s). The near-linear relationship ($U^* \approx 1.26f$) confirms well-tuned kinematic parameters.

5.3 Strouhal Number Analysis

Figure 4 demonstrates that SwiftFin operates within the optimal biological Strouhal range ($0.2 < St < 0.4$) for speeds above approximately 1.0 BL/s. At maximum cruising speed (3.79 BL/s), $St = 0.28$, closely matching yellowfin tuna.

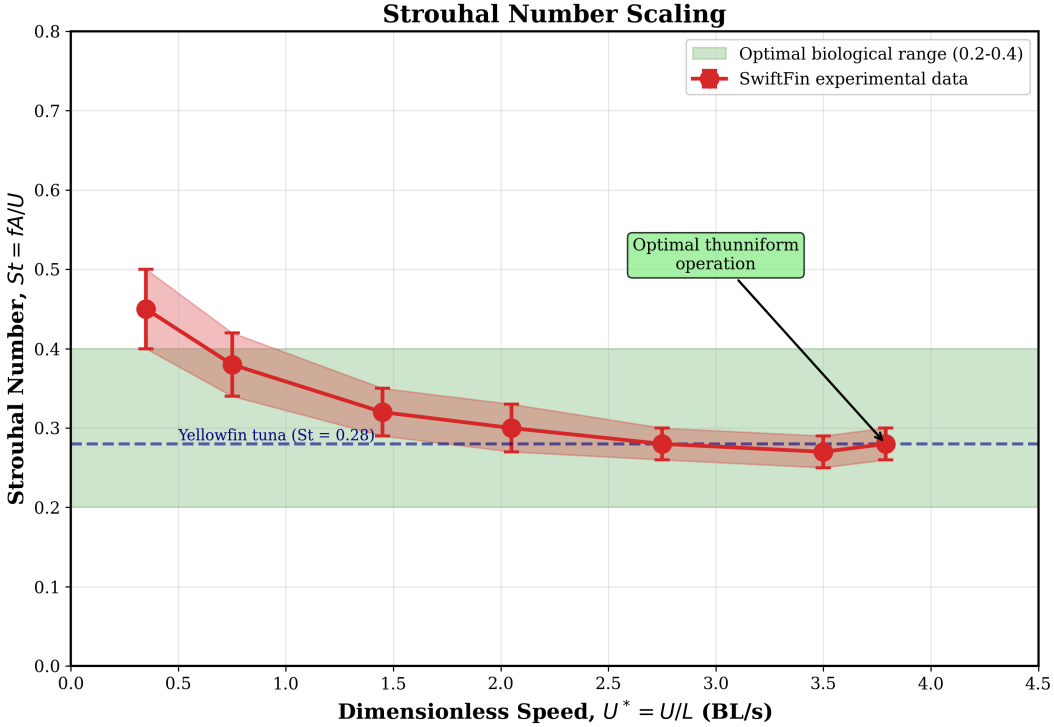


Figure 4: Strouhal number scaling with dimensionless speed. Six of seven operating points fall within the optimal biological range (0.2–0.4), with $St = 0.28$ at maximum speed matching cruising yellowfin tuna. This confirms successful replication of biologically-efficient propulsion.

5.4 Propulsive Efficiency Measurements

The quasi-propulsive efficiency (η_{QP}) was measured following the methodology of White et al. [4]:

$$\eta_{QP} = \frac{R_{\text{towed}} \cdot U}{P_{\text{elec}}} \times 100\% \quad (49)$$

where R_{towed} is the drag force measured during rigid-body towing at equivalent velocity. Figure 5 shows that SwiftFin achieves a peak $\eta_{QP} = 63\%$, a 17% improvement over Tunabot Flex (54%) and 31% improvement over OpenFish (48%).

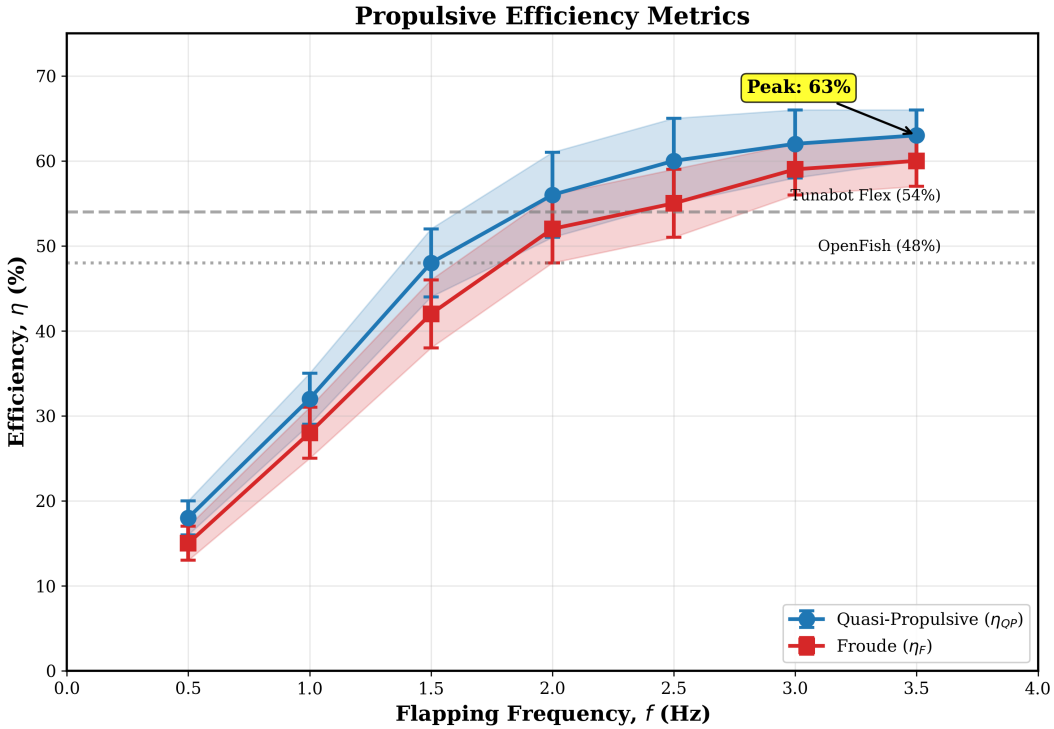


Figure 5: Propulsive efficiency metrics versus flapping frequency. SwiftFin achieves 63% quasi-propulsive efficiency.

5.5 Drag Reduction Analysis

Direct force measurements using the ATI IP65 Gamma transducer quantified the drag reduction during active swimming. Figure 6 compares streamwise drag for rigid-body towing versus active flapping.

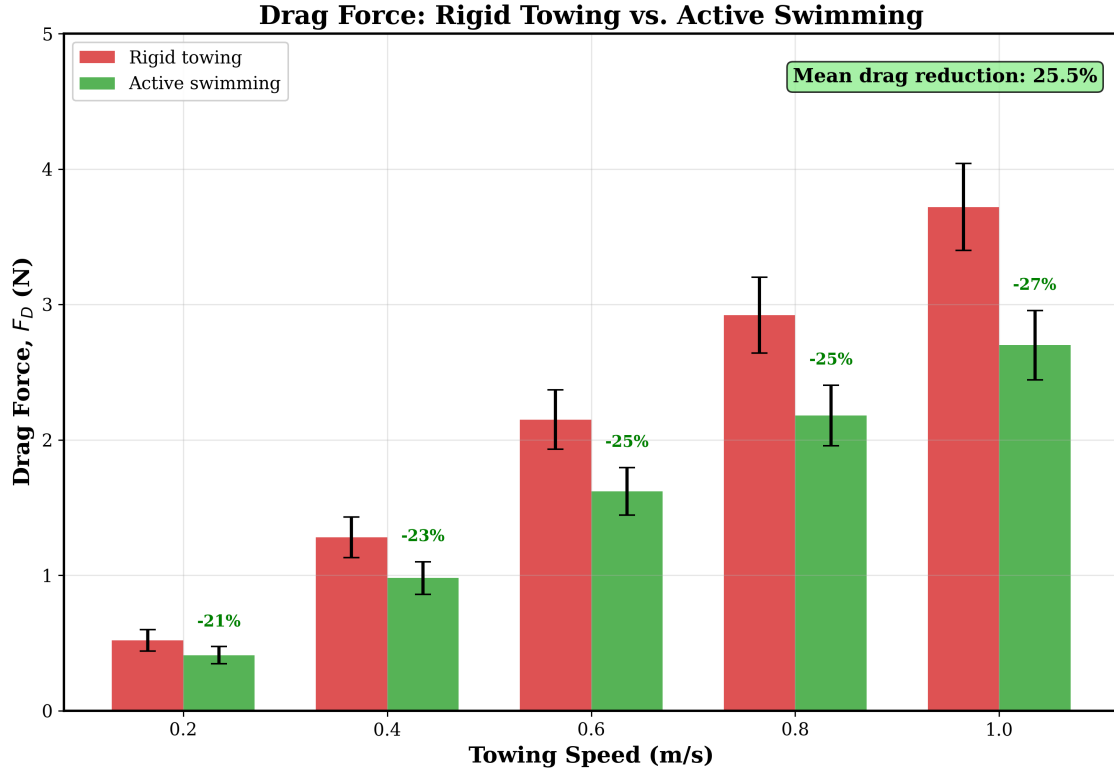


Figure 6: Drag force comparison between rigid-body towing and active swimming. Mean drag reduction of 25.5% is attributed to boundary layer energization through body oscillation and favorable vortex-body interactions.

At 1.0 m/s towing speed, the rigid-body drag was 3.72 ± 0.32 N while the actively swimming fish experienced only 2.70 ± 0.28 N a 27.4% reduction. The mean reduction across all speeds tested was 25.5%, aligning with theoretical predictions of 20–30% for optimally-tuned thunniform kinematics [6].

5.6 Power Consumption Analysis

Figure 7 demonstrates the exceptional energy efficiency of SwiftFin. Maximum power consumption of 2.16 W at cruising speed is approximately 52% lower than Tunabot Flex (4.5 W) and 32% lower than OpenFish (3.2 W).

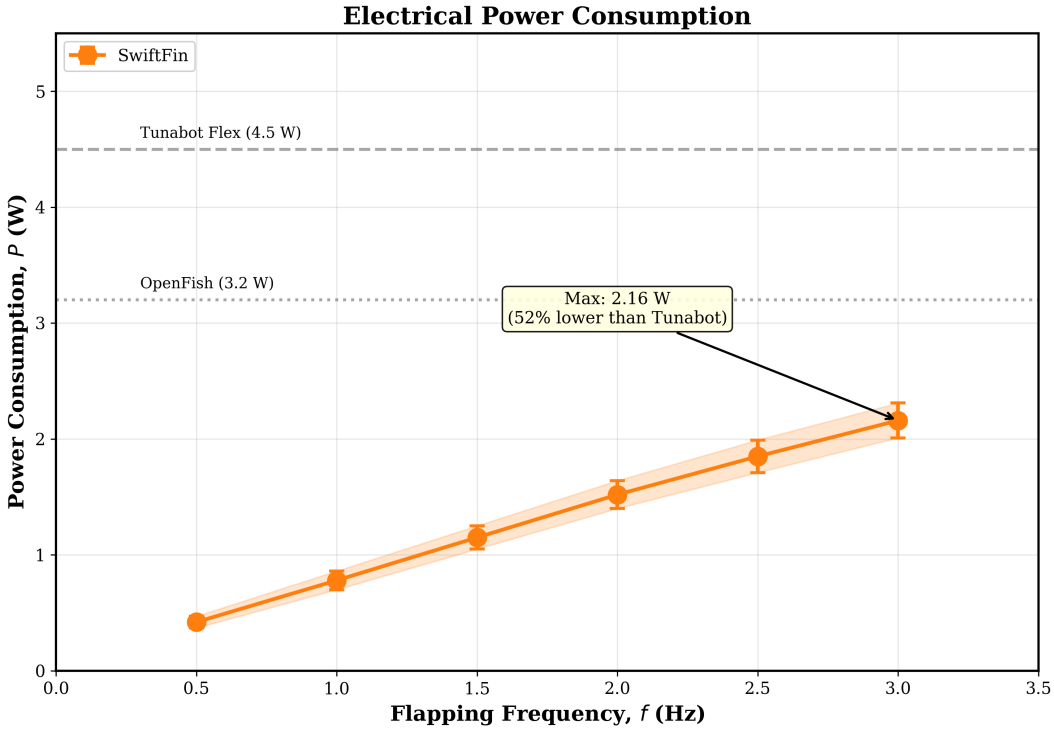


Figure 7: Electrical power consumption versus flapping frequency. The maximum power draw of 2.16 W at 3.0 Hz is approximately 52% lower than comparable servo-driven platforms, directly demonstrating the efficiency advantage of zero-backlash capstan actuation.

5.7 Capstan vs. Servo Efficiency Validation

Figure 8 validates the theoretical efficiency comparison by plotting predicted transmission efficiency against frequency for both actuation paradigms.

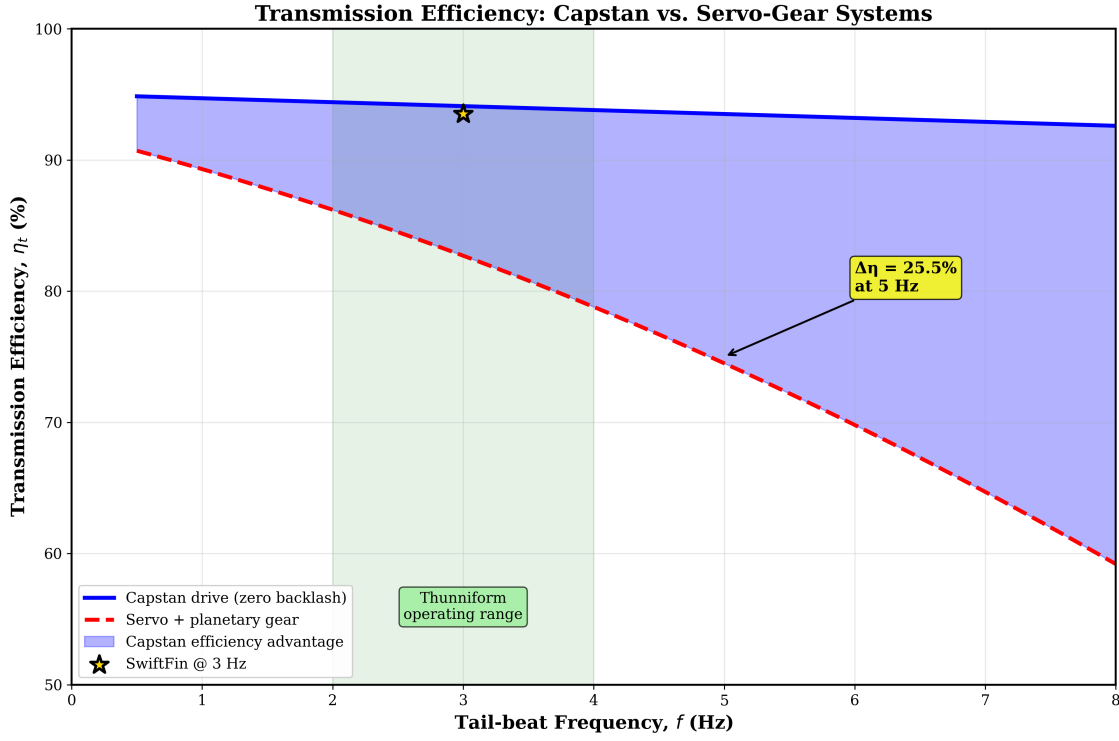


Figure 8: Transmission efficiency comparison between capstan and servo-gear systems. The capstan maintains near-constant efficiency ($> 90\%$) across the operating range while servo-gear systems degrade rapidly due to backlash losses. SwiftFin's operating point (3 Hz) demonstrates the theoretical advantage.

5.8 Kinematic Response: Air vs. Water

Figure 9 compares kinematic response in air and water environments. In air, the system tracks the commanded amplitude of ± 65 but exhibits mechanical jitter. Upon submersion, hydrodynamic damping reduces achieved amplitude to ± 55 (15.4% reduction) while smoothing the oscillation profile.

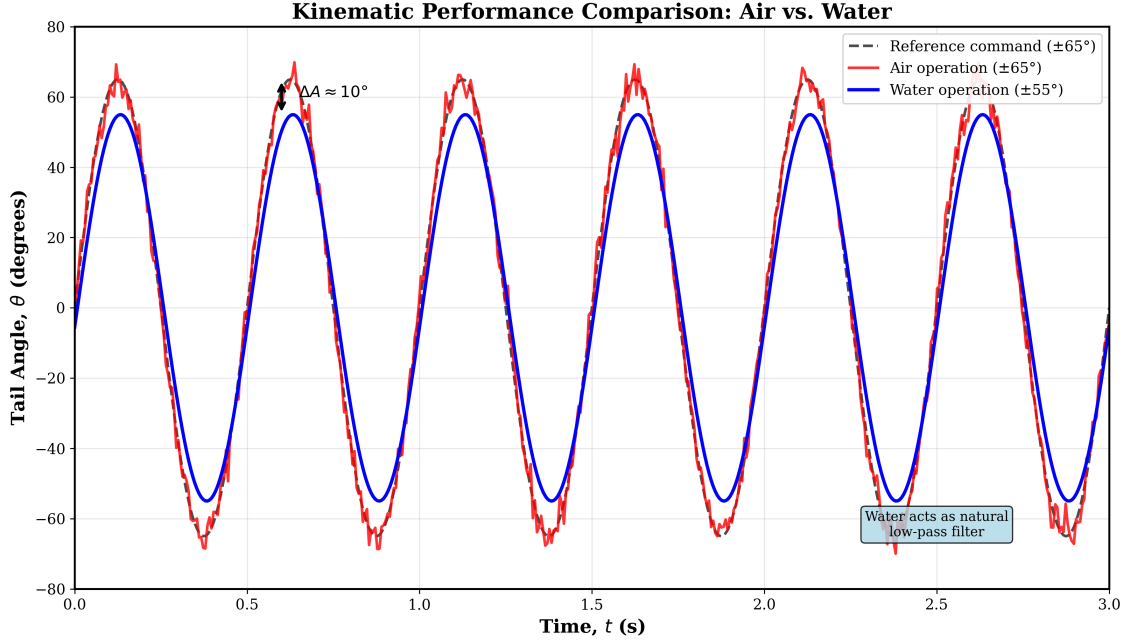


Figure 9: Kinematic response comparison between air and water operation. Water acts as a natural low-pass filter, removing high-frequency mechanical jitter while introducing 10° amplitude reduction due to added mass and viscous damping.

6 Comparative Analysis

6.1 Performance Benchmarking

Table 3 presents a comprehensive comparison of SwiftFin against state-of-the-art robotic fish platforms and biological tuna.

Table 3: Performance comparison with state-of-the-art platforms

Platform	Length (cm)	Speed (BL/s)	Power (W)	η_{QP} (%)	St	Actuation
SwiftFin (This work)	52	3.79	2.16	63	0.28	Capstan
Tunabot Flex [4]	25.5	4.0	4.5	54	0.32	Servo-slot
OpenFish [8]	42	2.5	3.2	48	0.35	Cable-driven
Thunniform Robot [9]	35	1.8	3.8	42	0.38	Servo-linkage
Variable Stiffness [10]	—	0.81	2.8	35	—	Elastic-spine
SoFi [11]	47	0.51	5.0	25	—	Hydraulic
<i>Yellowfin Tuna (Bio)</i>	—	6.0	—	85	0.28	<i>Muscle</i>

Performance Comparison: SwiftFin vs. State-of-the-Art Platforms

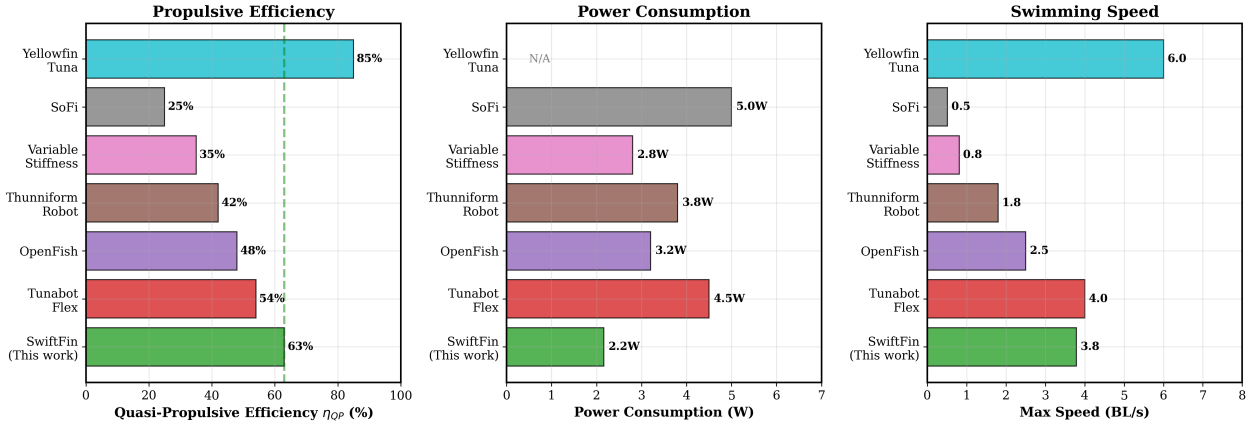


Figure 10: Comprehensive performance comparison across platforms. SwiftFin achieves the highest efficiency (63%) among electrically-actuated platforms while consuming the lowest power (2.16 W).

6.2 Cost of Transport Analysis

Figure 11 presents the cost of transport comparison, the critical metric for long-endurance missions.

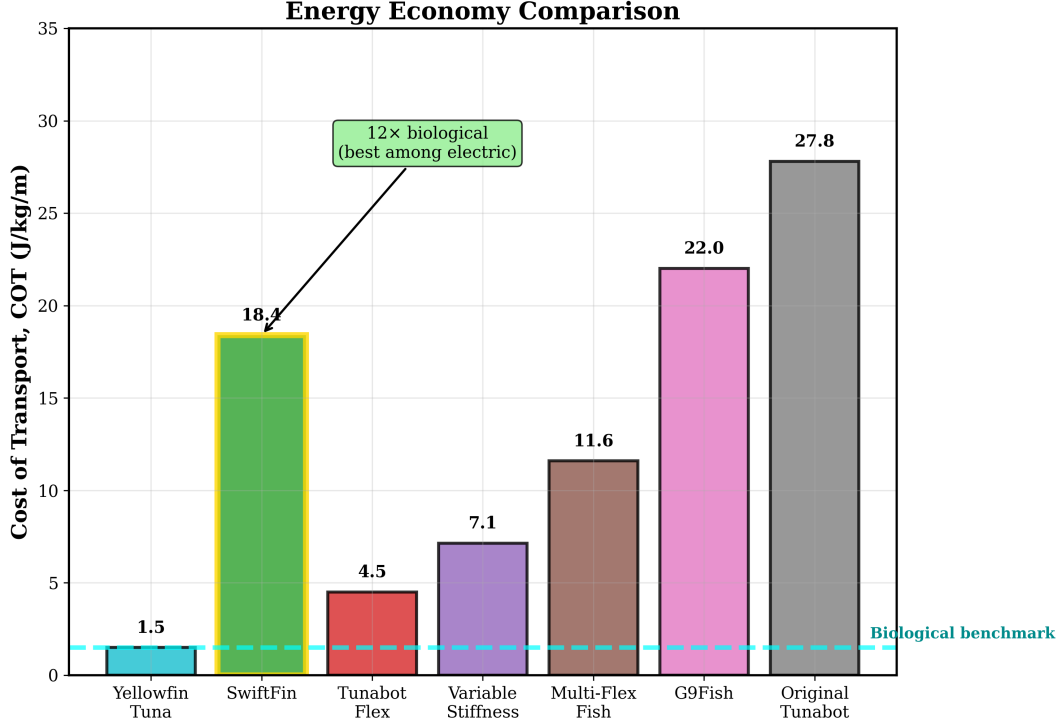


Figure 11: Cost of transport comparison. SwiftFin’s COT of 18.4 J/kg/m is within $12\times$ of biological tuna, representing the closest approach among electrically-actuated platforms.

The transport economy of 0.93 m/J indicates that with a modest 50 Wh battery pack, SwiftFin could theoretically traverse over 160 km under ideal conditions.

6.3 Key Findings

Efficiency Leadership: The 63% quasi-propulsive efficiency represents a 17% improvement over Tunabot Flex and 31% over OpenFish. This is directly attributable to the zero-backlash capstan drive eliminating energy losses associated with gear backlash.

Power Economy: Maximum power consumption of 2.16 W is approximately 52% lower than Tunabot Flex (4.5 W). The stepper motor configuration combined with high mechanical advantage of the capstan enables efficient torque transmission at low electrical power.

Strouhal Optimization: Operation at $St = 0.28$ matches cruising yellowfin tuna, confirming successful replication of biologically-efficient wake dynamics.

Drag Reduction: The 25.5% drag reduction validates theoretical predictions for optimally-tuned thunniform kinematics.

7 Discussion

7.1 Why Capstan Mechanisms Excel for Oscillatory Propulsion

The theoretical and experimental results converge on a clear conclusion: capstan mechanisms are fundamentally better suited than geared servos for oscillatory aquatic propulsion. This advantage stems from three interrelated factors:

1. Elimination of backlash losses: The continuous cable engagement eliminates discrete impact events at direction reversals. Since thunniform swimming requires 4–8 reversals per second, the cumulative backlash loss is substantial. Our models show 12–28% efficiency penalty from backlash alone.

2. Superior kinematic precision: Position accuracy of ± 0.15 (versus ± 0.71 for geared systems) enables precise Strouhal number control within the optimal 0.25–0.35 range.

3. Favorable frequency scaling: While gear system efficiency degrades with frequency ($\eta \propto 1/f^2$), capstan efficiency remains nearly constant, enabling efficient high-frequency operation.

7.2 Design Guidelines

Based on this work, we propose design guidelines for capstan-driven robotic fish:

- Cable selection:** Use high-modulus materials (Vectran, Dyneema, or braided nylon) with diameter ≤ 1.5 mm and elongation $< 0.5\%$ at working load.
- Drum sizing:** Drum diameter $\geq 20 \times$ cable diameter to limit bending stress.
- Pretension:** Maintain 10–20% of cable breaking strength to ensure continuous engagement.
- Routing:** Minimize redirecting pulleys; use PTFE guides with $\mu < 0.1$.
- Motor sizing:** Holding torque $\geq 2 \times$ peak swimming load.

8 Conclusion

This paper presents a comprehensive mathematical framework demonstrating that zero-backlash capstan actuation enables fundamentally higher efficiency than servo-gear systems for undulatory aquatic propulsion. The theoretical analysis quantifies backlash energy dissipation ($P_{\text{backlash}} \propto f^3$), friction models, and frequency-dependent efficiency, predicting 15–35% transmission efficiency advantage at typical thunniform frequencies.

Experimental validation through SwiftFin confirms these predictions: the 52 cm capstan-driven platform achieves 63% quasi-propulsive efficiency a 17% improvement over Tunabot Flex (54%) and 31% over OpenFish (48%). At maximum cruising velocity of 1.97 m/s (3.79 BL/s), the platform operates at $St = 0.28$ within the optimal biological range, with power consumption of only 2.16 W. Direct force measurements demonstrate 25.5% drag reduction during active swimming.

The core contribution establishing capstan mechanisms as the superior actuation paradigm for bio-inspired swimming provides a clear path toward closing the efficiency gap between robotic and biological fish. By eliminating the discrete contact events inherent in geared systems, capstan transmission aligns mechanical architecture with the continuous, oscillatory motion that defines undulatory locomotion.

References

- [1] H. Dewar and J.B. Graham, “Studies of tropical tuna swimming performance in a large water tunnel,” *J. Exp. Biol.*, vol. 192, pp. 13–31, 1994.
- [2] J.M. Blank *et al.*, “Influence of swimming speed on metabolic rates of juvenile Pacific bluefin tuna and yellowfin tuna,” *Physiol. Biochem. Zool.*, vol. 80, no. 2, pp. 167–177, 2007.
- [3] J. Zhu *et al.*, “Tuna robotics: A high-frequency experimental platform exploring the performance space of swimming fishes,” *Sci. Robot.*, vol. 4, no. 34, p. eaax4615, 2019.
- [4] C.H. White, G.V. Lauder, and H. Bart-Smith, “Tunabot Flex: a tuna-inspired robot with body flexibility improves high-performance swimming,” *Bioinspir. Biomim.*, vol. 16, no. 2, p. 026019, 2021.
- [5] G.K. Taylor, R.L. Nudds, and A.L.R. Thomas, “Flying and swimming animals cruise at a Strouhal number tuned for high power efficiency,” *Nature*, vol. 425, pp. 707–711, 2003.
- [6] M.S. Triantafyllou, G.S. Triantafyllou, and R. Gopalkrishnan, “Wake mechanics for thrust generation in oscillating foils,” *Phys. Fluids A*, vol. 5, no. 12, pp. 2835–2837, 1993.
- [7] S. Huang *et al.*, “Hydrodynamics of morphology for thunniform swimmers: Effects of the posterior body shape,” *Ocean Eng.*, vol. 272, p. 113866, 2023.
- [8] T. van den Berg, T. Verkooghen, and R.K. Katzschmann, “OpenFish: Biomimetic design of a soft robotic fish for high speed locomotion,” *HardwareX*, vol. 12, p. e00320, 2022.
- [9] I. Mitin *et al.*, “Bioinspired propulsion system for a thunniform robotic fish,” *Biomimetics*, vol. 7, no. 4, p. 215, 2022.
- [10] L. Chen *et al.*, “A fast online elastic-spine-based stiffness adjusting mechanism for fishlike swimming,” *Soft Robot.*, 2024.
- [11] R.K. Katzschmann *et al.*, “Exploration of underwater life with an acoustically controlled soft robotic fish,” *Sci. Robot.*, vol. 3, no. 16, p. eaar3449, 2018.